

Infrared Resonant Desorption of H₂O from Ice Multilayers

A. Krasnopoler^{†,‡} and S. M. George^{*,†}

Department of Chemistry and Biochemistry, University of Colorado, Boulder, Colorado 80309, and Duke Free Electron Laser Lab, Duke University, Durham, North Carolina 27708

Received: June 19, 1997; In Final Form: November 3, 1997

The resonant desorption of H₂O from ice multilayers was studied using a train of picosecond pulses from an infrared free electron laser. The infrared light was used to excite the O–H stretching vibration in H₂O in the ice multilayers and to cause H₂O resonant desorption. The H₂O resonant desorption spectrum was measured at infrared wavelengths between $\lambda = 2.8 \mu\text{m}$ and $\lambda = 3.4 \mu\text{m}$. The peak H₂O desorption yield occurred at $\lambda = 3.0 \mu\text{m}$. The H₂O resonant desorption spectrum was substantially enhanced relative to the infrared absorption spectrum of ice at infrared wavelengths shorter than $\lambda \sim 3.1 \mu\text{m}$. This enhancement was attributed to the melting of the ice film prior to H₂O desorption and the temperature-dependent absorption coefficient of the O–H stretching vibration. The H₂O desorption yields from 1 and 5 μm thick films were also measured at $\lambda = 2.94 \mu\text{m}$ and $\lambda = 3.09 \mu\text{m}$ for successive infrared pulses and versus pulse energy. The results were consistent with the melting of the ice film and the expected optical penetration depths in liquid water. Model calculations were in qualitative agreement with these experimental results and predicted H₂O desorption from a liquid H₂O film.

I. Introduction

Interest in ice has intensified recently because of the role of ice particles in the Antarctic ozone hole.^{1,2} Many questions have focused on ice surface chemistry.³ New techniques to investigate surface species on ice may lead to a better understanding of heterogeneous chemistry on ice. Methods to analyze ice have also become increasingly important for the study of ice core samples that contain a record of the earth's atmospheric history.⁴ New techniques that can monitor species in ice versus depth may help to understand the historical record that is trapped in ice cores.

The resonant desorption of H₂O from ice can provide a new technique for the analysis of ice surfaces. The optical penetration depth of infrared radiation in ice can also provide a means to desorb a well-defined increment of ice for depth-profiling analysis. To develop new surface and depth-profiling analysis methods, the infrared resonant desorption of H₂O from ice multilayers was studied using an infrared free electron laser (IRFEL). The IRFEL can excite the molecular vibrations of H₂O. If the H₂O molecule is adsorbed on a surface or in an ice multilayer film, this vibrational energy can promote desorption.^{5–7} Resonant desorption occurs if the H₂O molecule desorbs only when infrared light is resonant with one of its molecular vibrations.

Previous studies of H₂O resonant desorption have concentrated on the photoablation of biological samples because H₂O is also a major constituent of biological tissue. The optical characteristics of water have been employed to define the photoablation therapy.⁸ The photoablation studies have concentrated on the O–H stretching vibration in H₂O because this vibration has the maximum infrared absorption in liquid water at $\lambda \sim 2.94 \mu\text{m}$. At this wavelength, the imaginary refractive

index of $k \sim 1$ corresponds to an optical penetration depth $p = \lambda/4\pi k = \sim 1 \mu\text{m}$.^{8,9}

Most of the photoablation investigations have been conducted using the Er:YAG laser at $\lambda = 2.94 \mu\text{m}$.^{10,11} The short optical penetration depth of $p \sim 1 \mu\text{m}$ in water at $\lambda = 2.94 \mu\text{m}$ leaves thin zones of thermal collateral damage which is a desirable attribute for laser surgery. Minimal collateral damage would also be an asset during resonant desorption depth profiling of ice samples. The photoablation experiments have investigated the photoablation etch depth and have revealed the effects of the temperature-dependent absorption coefficient of the O–H stretching vibration.^{12,13} Other photoablation studies have utilized the IRFEL at $\lambda = 3 \mu\text{m}$.¹⁴

The present study of H₂O resonant desorption was performed in ultrahigh vacuum (UHV) on well-defined ice multilayers. The use of UHV enabled the desorption yield to be analyzed with a quadrupole mass spectrometer. These mass spectrometric measurements could determine the identity and magnitude of the desorption yield for each IRFEL pulse. The O–H stretching vibration in ice and liquid water has a broad infrared absorption spectrum. The tunability of the IRFEL allowed the H₂O resonant desorption to be studied over the entire absorption spectrum between $\lambda = 2.8 \mu\text{m}$ and $\lambda = 3.4 \mu\text{m}$.

II. Experimental Section

A schematic of the UHV chamber for the resonant desorption studies is shown in Figure 1. This chamber is equipped with a UTI-100C quadrupole mass spectrometer for the detection of desorption signals and residual gas analysis.⁵ A liquid nitrogen cryostat on a rotatable feedthrough provides for sample cooling and sample positioning inside the chamber.¹⁵ The chamber is pumped with both a turbomolecular pump and an ion pump. The turbomolecular pump provides for rapid transitions from atmospheric pressure to vacuum and also permits high gas throughput experiments. The ion pump is employed after the

[†] University of Colorado.

[‡] Duke University.

* To whom correspondence should be addressed.

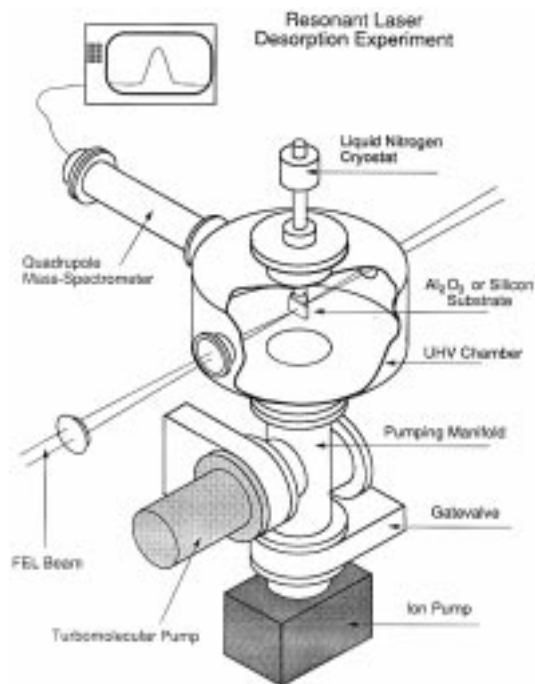


Figure 1. Experimental schematic of the UHV chamber for the resonant desorption experiments using the infrared free electron laser (IRFEL).

turbomolecular pump has reached high vacuum and allows the chamber to operate at UHV pressures.

A single-crystal Al₂O₃ substrate is mounted at the bottom of the liquid nitrogen cryostat.⁵ A chromium film was evaporated onto the backside of the Al₂O₃ crystal for resistive heating. For infrared transmission, a mask was utilized to define a clear circular window with a 5 mm diameter at the center of the substrate. A chromel–alumel thermocouple was attached to the front side of the Al₂O₃ crystal using a high-temperature ceramic adhesive (Aremco). This thermocouple provided an accurate measurement of the substrate temperature.

Ice films were grown by adsorbing H₂O at 140 K to deposit an ice film with the density of crystalline ice.¹⁶ Ice film thickness was monitored using optical interference techniques.¹⁷ A HeNe laser was incident at 45° at the center of the Al₂O₃ surface. The intensity of the reflected HeNe beam was measured by a photodiode and recorded by a computer. The photodiode signal versus time during ice film growth was analyzed and converted into an ice film thickness.¹⁷ After film growth, the Al₂O₃ substrate was cooled to the base temperature of 110 K for the H₂O resonant desorption experiments.

The Mark III IRFEL at Duke University is a continuously tunable infrared source that delivers a nearly diffraction-limited laser beam with extremely high peak power and average power.^{18,19} The Mark III IRFEL produces macropulses with a duration of ~3 μs that are composed of a train of micropulses. Each micropulse has a pulse width of ~2 ps and is separated from adjacent micropulses by ~350 ps. Consequently, there are approximately 8600 individual micropulses in one macropulse. Each macropulse typically has an energy of ~6 mJ. The macropulses can be produced at repetition rates up to 10 Hz. For this work, data were collected using a repetition rate of 1 Hz.

The spectral bandwidth of an IRFEL micropulse is ~0.5% of the wavelength or ~0.015 μm at λ = 3.0 μm. The frequency chirp during the IRFEL macropulse is ~0.5% of the wavelength or ~0.015 μm at λ = 3.0 μm. There is also a slight wavelength

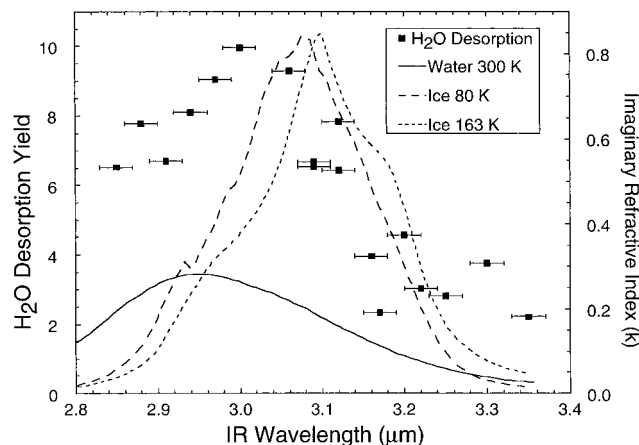


Figure 2. H₂O desorption yield (solid squares) from a 5 μm thick ice film at 110 K as a function of IR wavelength at a macropulse energy of 1 mJ. The imaginary index of refraction of amorphous ice deposited at 80 K [ref 20], polycrystalline ice deposited at 163 K [ref 21], and liquid water at 300 K [ref 9] are also shown for comparison.

drift of the IRFEL during the recording of the H₂O desorption yields at each given infrared wavelength. Consequently, the wavelength was checked before and after data acquisition to ensure that the wavelength did not drift excessively. Given these uncertainties, the estimated total uncertainty of the infrared wavelength is ±0.02 μm.

The beam from the IRFEL was focused using a 1 m CaF₂ lens. The IRFEL beam enters the chamber through a CaF₂ window. The focused beam on the Al₂O₃ substrate had a diameter (1/e) of ~600 μm. The beam is polarized and the total beam energy was controlled using a polarizer. The beam energy was measured using a pyrometer. The position of the beam on the Al₂O₃ sample was controlled by translating the 1 m CaF₂ lens in the horizontal and vertical directions.

For the resonant desorption experiment, a mechanical shutter was opened for 900 ms to allow only one IRFEL macropulse to impinge on the ice film on the Al₂O₃ substrate. The opening of the shutter was synchronized with the trigger pulse that initiates the generation of the IRFEL macropulse. Pressure bursts resulting from H₂O resonant desorption from the ice film were measured using the UTI-100C quadrupole mass spectrometer. H₂O was monitored at mass 18 and collected using a Labview data acquisition program. The H₂O pressure bursts in the vacuum chamber were observed to decay in ~10 ms.

III. Results

The H₂O resonant desorption yield versus IRFEL wavelength is shown by the solid squares in Figure 2. These results are for a 5 μm thick ice film at 110 K that was initially grown at 140 K. The H₂O desorption yield was determined from the peak of the H₂O pressure burst. The optical energy of the IRFEL macropulse was 1 mJ at each infrared wavelength. The wavelength uncertainty is indicated by the error bars in Figure 2. The wavelength was measured before and after data acquisition at each infrared wavelength. A similar resonant desorption spectrum was obtained for a 1 μm thick ice film at 110 K that was initially deposited at 140 K.

As the IRFEL wavelength decreases from λ = 3.4 μm, Figure 2 shows that the H₂O resonant desorption yield increases progressively. The peak H₂O desorption signal occurs at λ ~ 3.0 μm. The H₂O resonant desorption signal then decreases slowly for wavelengths less than λ ~ 3.0 μm. The H₂O desorption yield for each wavelength shown in Figure 2 was

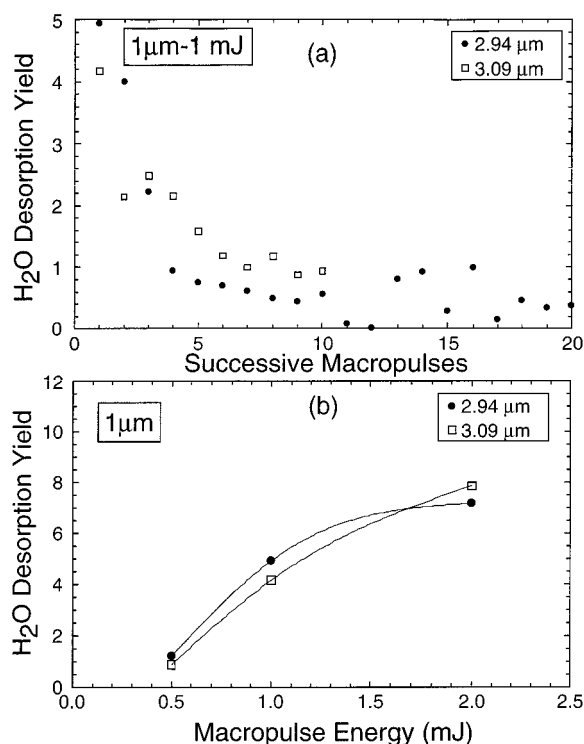


Figure 3. H₂O desorption yield from a 1 μm thick ice film at 110 K as function of (a) successive IRFEL macropulses at the same spatial location and (b) IRFEL macropulse energy at IR wavelengths of $\lambda = 2.94 \mu\text{m}$ and $\lambda = 3.09 \mu\text{m}$.

measured at a different spatial location on the ice film. The slight scatter in the H₂O desorption yield is attributed to the wavelength uncertainties and the energy fluctuations of the IRFEL macropulses.

The H₂O resonant desorption yield peaks at $\lambda \sim 3.0 \mu\text{m}$. In contrast, Figure 2 shows that the infrared absorption peaks occur at $\lambda = 3.08 \mu\text{m}$ for amorphous ice deposited at 80 K²⁰ and $\lambda = 3.10 \mu\text{m}$ for polycrystalline ice deposited at 163 K.²¹ This shift of the H₂O resonant desorption spectrum to shorter wavelengths is expected from the temperature-dependent absorption coefficient of the O–H stretching vibration.^{12,13} This shift moves the resonant desorption spectrum toward the infrared spectrum of liquid water. Figure 2 reveals that the absorption peak for liquid water at 300 K occurs at $\lambda = 2.94 \mu\text{m}$.⁹

For depth-profiling analysis of ice samples using H₂O resonant desorption, the infrared laser would remain at the same spatial location and consecutive laser pulses would progressively remove increments of the ice film. To evaluate the ability of the IRFEL to perform depth profiling of ice, the H₂O resonant desorption yield was measured for successive macropulses at the same spatial location for ice film thicknesses of 1 and 5 μm at infrared wavelengths of $\lambda = 2.94 \mu\text{m}$ and $\lambda = 3.09 \mu\text{m}$. The wavelengths of $\lambda = 2.94 \mu\text{m}$ and $\lambda = 3.09 \mu\text{m}$ correspond closely to the absorbance peaks in liquid water⁹ and polycrystalline ice,²¹ respectively. The wavelength of 2.94 μm also corresponds to the output wavelength of the Er:YAG laser. The optical penetration depths at $\lambda = 2.94 \mu\text{m}$ and $\lambda = 3.09 \mu\text{m}$ are $p = 0.99 \mu\text{m}$ and $p = 0.31 \mu\text{m}$, respectively, in polycrystalline ice.²¹ Likewise, the optical penetration depths at $\lambda = 2.94 \mu\text{m}$ and $\lambda = 3.09 \mu\text{m}$ are $d = 0.81 \mu\text{m}$ and $p = 1.26 \mu\text{m}$, respectively, in liquid water.⁹

For the 1 μm thick ice films and a macropulse energy of 1 mJ, the H₂O desorption yield in Figure 3a fell dramatically with successive macropulses at both $\lambda = 2.94 \mu\text{m}$ and $\lambda = 3.09 \mu\text{m}$. This behavior is consistent with the removal of a significant

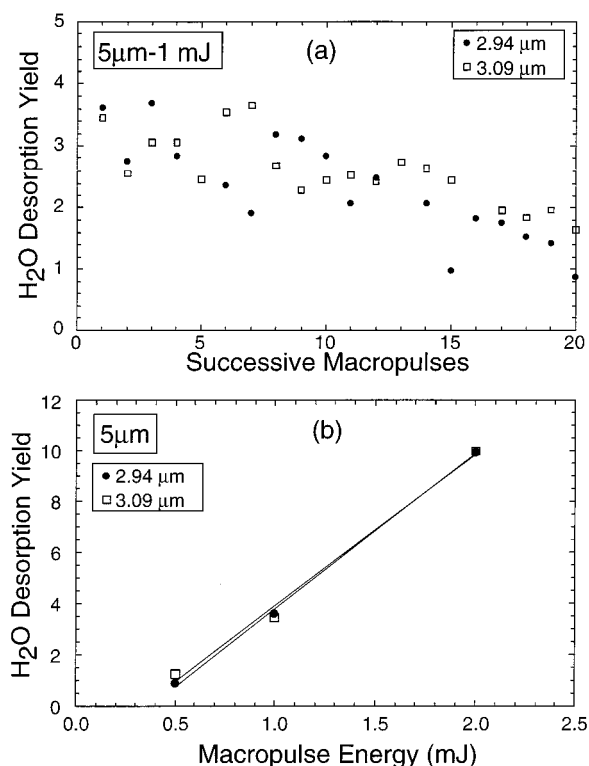


Figure 4. H₂O desorption yield from a 5 μm thick ice film at 110 K as function of (a) successive IRFEL macropulses at the same spatial location and (b) IRFEL macropulse energy at IR wavelengths of $\lambda = 2.94 \mu\text{m}$ and $\lambda = 3.09 \mu\text{m}$.

fraction of the 1 μm thick ice film by one macropulse. In contrast, the H₂O desorption yield in Figure 4a from the 5 μm thick films at a macropulse energy of 1 mJ was nearly constant for 5–10 macropulses before progressively decreasing with successive macropulses. This different behavior for the 5 μm thick films is expected because of its larger film thickness compared with the optical penetration depth. The initial H₂O desorption yields in Figure 4 for 1 mJ macropulse energies are not identical with those in Figure 2 at $\lambda = 2.94 \mu\text{m}$ and $\lambda = 3.09 \mu\text{m}$ because of different mass spectrometer sensitivities.

The suggestion that a significant fraction of the 1 μm thick ice film is removed at macropulse energies ≥ 1 mJ was confirmed by measuring H₂O resonant yields as a function of macropulse energy for ice film thicknesses of 1 and 5 μm . The initial H₂O desorption yields as a function of pulse energy at infrared wavelengths of $\lambda = 2.94 \mu\text{m}$ and $\lambda = 3.09 \mu\text{m}$ are shown in Figures 3b and 4b. Little difference is observed between the two infrared wavelengths of $\lambda = 2.94 \mu\text{m}$ and $\lambda = 3.09 \mu\text{m}$. However, there are differences between the two film thicknesses. For the 5 μm thick film, the H₂O desorption yield in Figure 4b increases linearly with pulse energy above a threshold macropulse energy. For the thinner 1 μm thick film, the H₂O desorption yield does not increase linearly at higher macropulse energies as shown in Figure 3b.

IV. Discussion

A. H₂O Resonant Desorption Spectrum. Figure 2 shows the comparison between the H₂O desorption yields and the imaginary component of the refractive index for amorphous and polycrystalline ice. The imaginary refractive index of liquid water is also shown for comparison. The peak of the H₂O desorption yield is scaled to be close to the largest imaginary refractive index for amorphous and polycrystalline ice. This

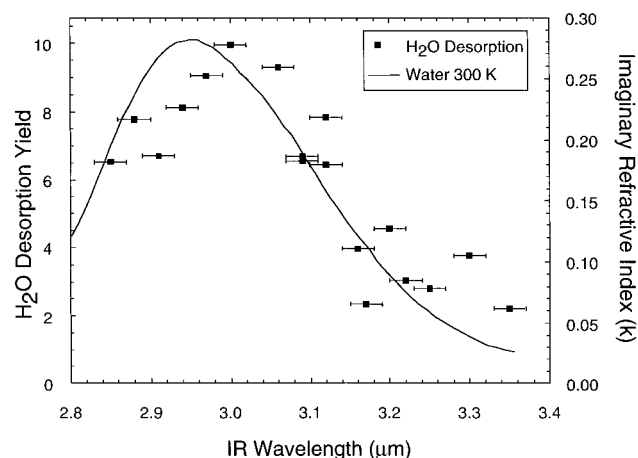


Figure 5. Detailed comparison of the H₂O desorption yield versus IR wavelength and the imaginary index of refraction of liquid water at 300 K [ref 9].

comparison shows that the peak in the H₂O resonant desorption spectrum at $\lambda = 3.0 \mu\text{m}$ falls between the absorption peaks in polycrystalline ice²¹ and liquid water.⁹

At infrared wavelengths between $\lambda = 3.06$ and $\lambda = 3.24 \mu\text{m}$, there is reasonable agreement between the resonant desorption spectrum and the infrared absorption spectrum for ice. At wavelengths greater than $\lambda = 3.24 \mu\text{m}$, the H₂O desorption yield is slightly greater than expected based on the infrared absorption spectrum of ice. At wavelengths shorter than the peak in the ice spectra at $\lambda \sim 3.1 \mu\text{m}$, the H₂O desorption yield is enhanced relative to the infrared absorption spectrum of ice.

The IRFEL macropulse consists of a $\sim 3 \mu\text{s}$ train of ~ 8600 micropulses. If the first micropulse does not induce a temperature rise sufficient to cause H₂O desorption, the successive micropulses will be irradiating a progressively warmer ice film. The enhancement of the desorption yield for $\lambda < 3.1 \mu\text{m}$ may be explained by the change in the absorption coefficient for the O–H stretching vibration during the heating of the ice film.^{12,13} This “dynamic absorption coefficient” is attributed to the weakening of the hydrogen-bonding network versus temperature.^{12,13,22,23}

Spectral shifts to shorter wavelength versus temperature are observed for the O–H stretching vibration of HDO in polycrystalline ice.²⁴ The peak absorption shifts from $\lambda = 3.06 \mu\text{m}$ at 16 K to $\lambda = 3.02 \mu\text{m}$ at 273 K. The spectral shift to shorter wavelengths with increasing temperature continues in liquid water.^{22,23} At a pressure of 250 bar, the absorption peak for the O–H stretching vibration in HDO shifts from $\lambda = 2.94 \mu\text{m}$ at 293 K to $\lambda = 2.74 \mu\text{m}$ at 773 K.²³ The O–H stretching absorption peak also becomes broader and decreases in intensity.

The peak of the H₂O resonant desorption yield at $\lambda = 3.0 \mu\text{m}$ is close to the infrared absorption peak at $\lambda = 2.94 \mu\text{m}$ for liquid H₂O at 300 K. If more infrared energy is absorbed by a liquid water film than a solid ice film, the H₂O resonant desorption spectrum should more closely resemble the infrared spectrum of liquid water. A more detailed comparison of the H₂O desorption yields and the infrared spectrum of liquid water at 300 K is shown in Figure 5. The peak of the H₂O resonant desorption yield is scaled to be close to the peak of the infrared spectrum of liquid water.

Figure 5 reveals a close correspondence between the H₂O desorption yield and the infrared spectrum of liquid water. This similarity argues that the ice film melts and exists in the liquid state during a significant fraction of the total time that the film is heated by the IRFEL macropulse. However, the peak of the

H₂O desorption yield at $\lambda = 3.0 \mu\text{m}$ is between the absorption peak for liquid water at $\lambda = 2.94 \mu\text{m}$ and the absorption peak for polycrystalline ice at $\lambda = 3.10 \mu\text{m}$. This peak position argues that the H₂O resonant desorption spectrum contains contributions from the infrared absorbance of both liquid water and solid ice.

Despite the difference between the imaginary refractive indices and the optical penetration depths at $\lambda = 2.94 \mu\text{m}$ and $\lambda = 3.09 \mu\text{m}$, the absolute H₂O desorption yields in Figures 3 and 4 are comparable for these two wavelengths at the same macropulse energy. Similar H₂O desorption yields may be rationalized from the infrared absorption spectra for ice and liquid water. Although infrared light at $\lambda = 3.09 \mu\text{m}$ has the largest imaginary refractive index for ice, Figure 2 indicates that the imaginary refractive index at $\lambda = 3.09 \mu\text{m}$ will decrease when the ice melts. After melting, the imaginary refractive index at $\lambda = 3.09$ is comparable to the imaginary index at $\lambda = 2.94 \mu\text{m}$. In contrast, only a small increase in the imaginary refractive index will be observed at $\lambda = 2.94 \mu\text{m}$ when the ice melts.

A smaller imaginary refractive index, k , or a longer optical penetration depth, $p = \lambda/4\pi k$, will enable the infrared light to penetrate deeper into the ice film. This larger penetration depth will lower the heat dissipated per volume and reduce the H₂O desorption yield. Although the ice film will be initially heated more quickly at $\lambda = 3.09 \mu\text{m}$, the heating rates for $\lambda = 3.09 \mu\text{m}$ and $\lambda = 2.94 \mu\text{m}$ will be more comparable at higher temperatures. After the ice film melts, the optical penetration depths at $\lambda = 2.94 \mu\text{m}$ and $\lambda = 3.09 \mu\text{m}$ both will continue to increase with temperature as the absorbance of the O–H stretching vibration shifts to shorter wavelengths.^{12,13,22,23}

Similar temperature-dependent changes in the absorption coefficient of the O–H stretching vibration are observed during laser photoablation with an Er:YAG laser.^{12,13} For laser pulse irradiation using an Er:YAG laser at $\lambda = 2.94 \mu\text{m}$ or an Er:YSGG laser at $\lambda = 2.79 \mu\text{m}$, the temperature-dependent effects limit the H₂O absorption coefficient. Compared with the expected optical penetration depth based on measured absorption coefficients, larger optical penetration depths and ablation etch depths are observed at higher laser pulse energies.^{12,13} These effects are attributed to absorption peak shifts to shorter wavelengths caused by the “dynamical” absorption coefficient.

B. H₂O Desorption Yields for Successive Macropulses.

The H₂O desorption yields from successive macropulses for the 1 and 5 μm films shown in Figures 3a and 4a display the effect of the optical penetration depth. For the 1 μm film, the film thickness is comparable to the initial optical penetration depth. Consequently, infrared laser energy is absorbed down to the sapphire substrate. The sharp decrease in H₂O desorption yield in Figure 3a with successive macropulses suggests that the desorption depth is close to the 1 μm film thickness. The nonlinear increase in H₂O desorption yield with macropulse energy displayed in Figure 3b also suggests that a significant fraction of the ice film is removed at macropulse energies ≥ 1 mJ. After the ice film is removed at the center of the focused infrared laser beam, additional increases in the H₂O desorption yield result only from a widening of the desorption area.²⁵

In contrast, the 5 μm film is much thicker than the optical penetration depth. Consequently, the infrared laser energy is not absorbed throughout the entire film thickness. This behavior is reflected in the nearly constant H₂O desorption yield with successive macropulses displayed in Figure 4a. The linear increase in the H₂O desorption yield with increasing macropulse

TABLE 1: Parameters in the Finite Element Model^a

symbol	definition	value
T_i	temperature	variable
z	depth	variable
r	radial distance	variable
t	time	variable
α_i	thermal diffusivity	$\alpha_1 = 0.06325 \text{ cm}^2/\text{s}$, $\alpha_2 = 0.1396 \text{ cm}^2/\text{s}$
J_0	micropulse fluence	$2.32 \times 10^7 \text{ J}/(\text{cm}^2 \text{ s})$
μ	IR absorbance	$1 \mu\text{m}^{-1}$
d	film thickness	1 or $5 \mu\text{m}$
r_p	1/e laser spot radius	$300 \mu\text{m}$
t_p	micropulse width	2 ps
t_w	micropulse spacing	350 ps
T_0	initial temperature	110 K
κ_i	thermal conductivity	$\kappa_1 = 0.050 \text{ W}/(\text{m K})$, $\kappa_2 = 0.419 \text{ W}/(\text{m K})$
ν	preexponential factor	$2.8 \times 10^{30} \text{ molecules}/(\text{cm}^2 \text{ s})$
E_d	heat of adsorption	49.8 kJ/mol
N_A	Avogadro's number	6.02×10^{23}
R	ideal gas constant	$8.314 \text{ J}/(\text{mol K})$

^a The subscripts "1" and "2" designate the ice film and sapphire substrate, respectively. Literature values were employed for the thermal conductivity and diffusivity²⁷ and H₂O desorption kinetics from ice.¹⁷

energy shown in Figure 4b is also consistent with a film thickness that is much greater than the optical penetration depth.

C. Model Calculations. To understand the differences between the results for the 1 and $5 \mu\text{m}$ thick films, a finite difference model was constructed to calculate the temperature rise in the ice film during excitation by the IRFEL macropulse. The model solved the heat equation for the ice film:

$$\frac{\partial T_1}{\partial t} = \alpha_1 \frac{\partial^2 T_1}{\partial z^2} + \mu J_0 \sum_{i=1}^N \exp\left(-\mu z - \left(\frac{r}{r_p}\right)^2 - \frac{t - it_w}{t_p}\right) \quad 0 \leq z < d \quad (1)$$

The heat equation for the sapphire substrate is given by

$$\frac{\partial T_2}{\partial t} = \alpha_2 \frac{\partial^2 T_2}{\partial z^2} \quad z \geq d \quad (2)$$

The definitions of the parameters and their values are given in Table 1. The subscripts "1" and "2" designate the ice film and sapphire substrate, respectively.

The IRFEL macropulse was modeled as a series of 8600 micropulses with Gaussian radial and temporal line shapes. Each micropulse was separated from adjacent micropulses by 350 ps. The energy in the total macropulse was 1 mJ, and the energy in each micropulse was $116 \mu\text{J}$. Absorbance in the z direction decays exponentially according to the optical penetration depth of $p = \lambda/4\pi k$. Radial heat conduction was neglected because the thickness of the film, d , is small with respect to the radius of the focused laser beam, r_p . The absorption coefficient, μ , was assumed to be independent of temperature.

Solving eqs 1 and 2 requires initial and boundary conditions. The temperature is equal to the initial temperature, T_0 , throughout the film and substrate at $t = 0$: $T_1(t=0, z) = T_2(t=0, z) = T_0$. At the surface of the film at $z = 0$, the heat flux out of the film is caused by H₂O desorption:

$$\frac{\partial T_1}{\partial z}\bigg|_{z=0} = -\frac{\nu E_d}{\kappa_1 N_A} \exp\left(-\frac{E_d}{RT_1}\right) \quad (3)$$

At the interface between the film and the substrate ($z = d$), the temperatures are the same: $T_1(t, z=d) = T_2(t, z=d)$. The heat

flux between the ice and sapphire is also equal:

$$\kappa_1 \frac{\partial T_1}{\partial z}\bigg|_{z=d} = \kappa_2 \frac{\partial T_2}{\partial z}\bigg|_{z=d} \quad (4)$$

Given that the sapphire substrate is much thicker than the ice film, the sapphire substrate temperature is $T_2 = T_0$ when $z \rightarrow \infty$.

The partial differential equations and the initial and boundary conditions were nondimensionalized using characteristic length, time, and temperature scales, and the partial differential equations were converted to difference equations for use in the finite element model. The temperature in the film and substrate was calculated by the implicit method.²⁶ For each time step, a tridiagonal matrix was created to solve the nondimensional difference forms of eqs 1 and 2 for each volume element at constant r .

To include H₂O desorption in the continuum approach of the finite element model, the heat flux at the surface was set equal to zero until the mass flux from the topmost volume element was sufficient to desorb the entire volume element. The mass flux was calculated using the zero-order desorption kinetics for H₂O from ice multilayers.¹⁷ The total mass flux for each surface element was updated after each time step. Desorption occurred when the total mass desorbed exceeded the total mass in the volume element and the heat of desorption was accounted for according to eq 3. With the desorption of the topmost volume element, the adjacent element became the new topmost element and the accumulated mass flux was reset to zero.

The film thickness and substrate were each divided into 500 spatial increments in the z direction. Ten radial increments were used to describe the Gaussian spatial profile in the r direction. The time step was 0.5 ps. The absorption coefficient was $1 \mu\text{m}^{-1}$. This absorption coefficient corresponds to the absorbance in polycrystalline ice at $\lambda = 2.94 \mu\text{m}$.²¹ This wavelength was chosen for comparison with the experimental results and because there is little change in the absorption coefficient between ice and water at $\lambda = 2.94 \mu\text{m}$. The two film thicknesses studied were 1 and $5 \mu\text{m}$. The thickness of the substrate was $2000 \mu\text{m}$, and the initial temperature was 110 K. The physical properties of ice and sapphire were all assumed to be independent of temperature. All parameters were defined at the initial temperature of 110 K and are summarized in Table 1.

The temperature profiles at the center of the laser profile in the 1 and $5 \mu\text{m}$ films are shown in Figures 6 and 7. These temperatures occur immediately after the passage of the peak of the micropulse through the film. Results are shown after the 1st, 11th, 101st, and 501st micropulses. The position in the film is scaled by the film thickness for comparison of the $d = 1 \mu\text{m}$ and $d = 5 \mu\text{m}$ films.

After the first micropulse shown in Figure 6a, the temperature at the surface is the same for both film thicknesses. However, the effect of the ratio of the film thickness to optical penetration depth is readily apparent. For the $1 \mu\text{m}$ thick film, the temperature is higher than 110 K throughout the entire film. A sharp drop in the temperature is observed at the ice–sapphire interface because no infrared light is absorbed by the sapphire substrate. In the $5 \mu\text{m}$ film, the temperature decreases more rapidly with normalized position in the film, and the ice–sapphire interface temperature remains close to the initial temperature of 110 K.

The temperature profile after 11 micropulses is shown in Figure 6b. The surface temperatures are still about the same for the 1 and $5 \mu\text{m}$ films with an increase to almost 120 K. The noticeable difference is the temperature drop for the $1 \mu\text{m}$ film

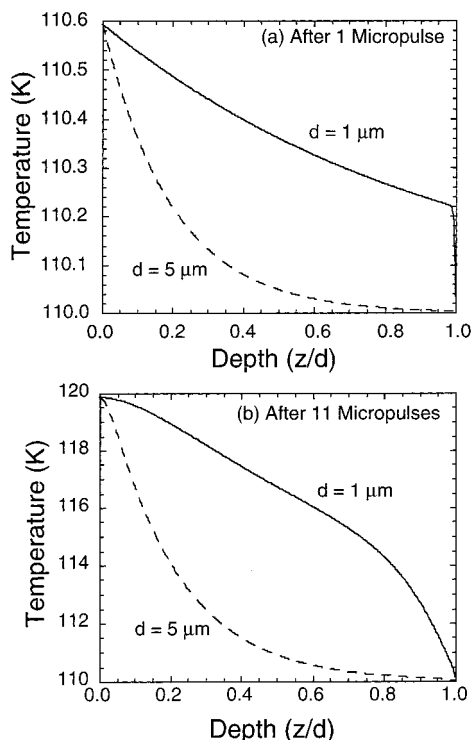


Figure 6. Temperature profile as a function of depth at the center of the focused laser pulse as calculated by a finite element model after (a) 1 micropulse and (b) 11 micropulses. Results are for a 1 mJ macropulse with an optical penetration depth of $1 \mu\text{m}$ for film thicknesses of 1 and $5 \mu\text{m}$.

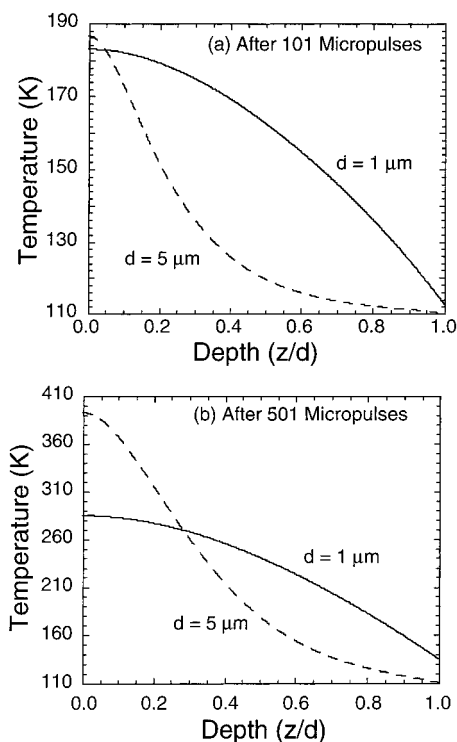


Figure 7. Temperature profile as a function of depth at the center of the focused laser pulse as calculated by a finite element model after (a) 101 micropulses and (b) 501 micropulses. Results are for a 1 mJ macropulse with an optical penetration depth of $1 \mu\text{m}$ for film thicknesses of 1 and $5 \mu\text{m}$.

at distances $<0.2 \mu\text{m}$ from the sapphire substrate. This temperature decrease is attributed to cooling by the substrate. For a thermal diffusivity of $D = 6.325 \times 10^{-2} \text{ cm}^2/\text{s}$,²⁷ the

mean-squared heat displacement is $x = (2Dt)^{1/2}$ or $x = 0.066 \mu\text{m}$ in $t = 350 \text{ ps}$ during the time between adjacent micropulses or $x = 0.21 \mu\text{m}$ in $t = 3500 \text{ ps}$ during the time required for the passage of 11 micropulses.

After 101 micropulses, the temperature profile shown in Figure 7a indicates that the surface temperature of the $5 \mu\text{m}$ film exceeds the surface temperature of the $1 \mu\text{m}$ film. This effect results from cooling by the sapphire substrate. Thermal diffusion to the substrate occurs more readily in the $1 \mu\text{m}$ film and results in greater cooling between micropulses. The more rapid cooling in the $1 \mu\text{m}$ film was also observed by monitoring the surface temperature as a function of time. Although the temperature rise immediately after the first micropulse is similar as shown in Figure 6a, the $5 \mu\text{m}$ film heats much more quickly because of the slower cooling between micropulses.

The thicker $5 \mu\text{m}$ film provides much greater thermal isolation from the sapphire substrate. Figure 7b shows that the temperature of the surface of the $5 \mu\text{m}$ film is nearly 100 K higher than the $1 \mu\text{m}$ film after 501 micropulses. However, the $1 \mu\text{m}$ film is still hotter at the ice-sapphire interface. The surface of the sapphire substrate is close to the initial temperature of 110 K for the $5 \mu\text{m}$ film after 501 micropulses.

The more uniform heating of the $1 \mu\text{m}$ film agrees well with the H₂O desorption yield results for successive macropulses shown in Figure 3a. Most of the H₂O in the irradiated area on the ice film is removed during the first macropulse. In contrast, the macropulse does not penetrate as deeply in the $5 \mu\text{m}$ film. Consequently, more laser macropulses are required to remove all the H₂O in the irradiated area as shown in Figure 4a.

The results of Figure 3a suggest that an IRFEL macropulse with a pulse energy of $\sim 1 \text{ mJ}$ is able to desorb an ice film with a $\sim 0.5 \mu\text{m}$ thickness. Together with the desorption kinetics of H₂O from ice multilayers and the pulse length of the macropulse, this observation can be used to obtain an estimate of an average ice film temperature during resonant desorption. The zero-order desorption kinetics of H₂O from ice multilayers are $-d\Theta/dt = 2.8 \times 10^{30} \text{ molecules}/(\text{cm}^2 \text{ s}) \exp[-11.9 \text{ kcal/mol}/RT]$.¹⁷ Assuming that $\Delta\Theta = 0.5 \mu\text{m thickness} = 1.54 \times 10^{18} \text{ molecules}/\text{cm}^2$ and $\Delta t = 1 \mu\text{s}$, these desorption kinetics yield a ice film temperature of $\sim 420 \text{ K}$. Because the film is heated continuously during the IRFEL macropulse, this estimated desorption temperature is a lower limit for the highest desorption temperature.

The model calculations can also be utilized to determine the H₂O desorption temperature. Using the same zero-order H₂O desorption kinetics as given above, the model yields the desorption of the first Δz volume element in the $1 \mu\text{m}$ film at 337 K. This desorption occurs after 450 ns or approximately 1285 micropulses. Likewise, the desorption of an equivalent volume element in the $5 \mu\text{m}$ film occurs at 377 K. This desorption occurs after 162 ns or approximately 463 micropulses. The higher temperature and shorter time required for desorption from the thicker $5 \mu\text{m}$ film may be understood in terms of the effect of heating rate on desorption yield. A higher heating rate results in a higher desorption temperature required for a particular desorption yield because there is less time for desorption at a given temperature.²⁸

The calculated onset of desorption at 337 K is in fairly good agreement with the estimated desorption temperature of 420 K for a $0.5 \mu\text{m}$ thick film to desorb in $1 \mu\text{s}$. However, the model also predicts that the $5 \mu\text{m}$ thick ice film will completely desorb before the end of the first macropulse. This prediction disagrees with the experimental results in Figure 4a. This disagreement may be expected because the model calculations do not account

for the temperature dependence of the absorption coefficient or any other parameter.

In addition to the neglect of the temperature-dependent parameters, the model does not take into account possible effects resulting from light scattering or absorption by desorbing material. The model also assumes a static ice film. If the ice film melts, the liquid film may flow and refill the desorption area. The model is very simple, and the processes occurring during infrared laser resonant desorption may be more complex. However, the model does give an estimate for the temperatures that are required to reach the onset of desorption. The predicted onset of H₂O desorption at $T > 330$ K is consistent with the melting of the ice film prior to H₂O desorption.

Based on the infrared absorption spectra for the O—H stretching vibration in HDO at a pressure of 250 bar,²² a desorption temperature of ~ 420 K would correspond to an absorption peak at $\lambda \sim 2.9$ μm . Because most of the infrared energy should be absorbed at temperatures below the desorption temperature, this predicted absorption peak at $\lambda = 2.9$ μm is a lower limit for the peak of the H₂O resonant desorption spectrum. In agreement with this prediction, the peak of the H₂O resonant desorption spectrum at $\lambda = 3.0$ μm corresponds to a temperature that is intermediate between the initial temperature of 110 K and a desorption temperature of ~ 420 K.

V. Conclusions

The resonant desorption spectrum of H₂O from ice multilayers from $\lambda = 2.8 - 3.4$ μm was measured using a tunable infrared free electron laser (IRFEL). Resonant infrared excitation of the O—H stretching vibration heated the ice film and promoted H₂O desorption. The resonant desorption spectrum was not identical with the infrared absorption spectrum of ice. Much higher H₂O desorption signals were obtained than expected at IRFEL wavelengths shorter than the peak of the infrared absorption spectrum at $\lambda \sim 3.1$ μm . This shift of the resonant desorption spectrum to shorter wavelengths was explained by the melting of the ice film and the temperature-dependent absorption coefficient of the O—H stretching vibration. The phase change and temperature increase disrupts the H₂O hydrogen-bonding network and shifts the absorption of the O—H stretching vibration to shorter wavelengths.

The H₂O desorption yields versus successive infrared macropulses at both $\lambda = 2.94$ μm and $\lambda = 3.09$ μm were measured for 1 and 5 μm thick ice films. Similar H₂O desorption yields and desorption etch depths were observed at $\lambda = 2.94$ μm and $\lambda = 3.09$ μm . These results were in agreement with the melting of the ice film. Model calculations helped to explain the differences between the 1 and 5 μm thick ice films and were consistent with H₂O desorption from a melted liquid ice film. This study has shown that infrared resonant desorption can

effectively remove H₂O from ice multilayers. This resonant desorption method may be useful to remove surface species from ice to study heterogeneous chemistry on ice. H₂O resonant desorption may also provide a convenient new method to perform depth profiling of ice samples to analyze species trapped in ice cores.

Acknowledgment. This work was supported by the National Science Foundation under Grant CHE-9528473 and the Office of Naval Research through Grant N00014-96-1-1297. The authors acknowledge Dr. O. Sneh for help building the UHV chamber for these resonant desorption studies. The authors would also like to thank Dr. K. David Straub and Prof. John M. J. Madey and their research team at the Duke Free Electron Laser Center.

References and Notes

- (1) Solomon, S.; Garcia, R. R.; Rowland, F. S.; Wuebbles, D. J. *Nature* **1986**, *321*, 755.
- (2) Solomon, S. *Nature* **1990**, *347*, 347.
- (3) Tabazadeh, A.; Turco, R. P. *J. Geophys. Res.* **1993**, *98*, 12727.
- (4) *Chemical Exchange between the Atmosphere and Polar Snow*; Wolff, E. W., Bales, R. C., Eds.; NATO ASI Series, Series I, Global and Environmental Change, Vol. 43; Springer-Verlag: Berlin, 1996.
- (5) Tro, N. J.; Arthur, D. A.; George, S. M. *J. Chem. Phys.* **1989**, *90*, 3389.
- (6) Chan, K.-C.; Donsig, H. A.; Ranier, D.; Brown, L. S. *J. Vac. Sci. Technol. A* **1993**, *11*, 2084.
- (7) Peremans, A.; Dereux, A.; Maseri, F.; Darville, J.; Gilles, J.-M.; Vigneron, J.-P. *Phys. Rev. B* **1992**, *45*, 8598.
- (8) Wolbarsht, M. L. *IEEE J. Quantum Electron.* **1984**, *QE-20*, 1427.
- (9) Downing, H. D.; Williams, D. J. *Geophys. Res.* **1975**, *80*, 1656.
- (10) Walsh, J. T., Jr.; Flotte, T. J.; Deutsch, T. F. *Lasers Surg. Med.* **1989**, *9*, 314.
- (11) Walsh, J. T., Jr.; Deutsch, T. F. *Lasers Surg. Med.* **1989**, *9*, 327.
- (12) Cummings, J. P.; Walsh, J. T., Jr. *Appl. Phys. Lett.* **1993**, *62*, 1988.
- (13) Walsh, J. T., Jr.; Cummings, J. P. *Lasers Surg. Med.* **1994**, *15*, 295.
- (14) Hoke, J. A.; Burkes, E. J., Jr.; Gomes, E. D.; Hooper, B. A.; Walbarsht, M. L. *Lasers Life Sci.* **1995**, *6*, 251.
- (15) George, S. M. *J. Vac. Sci. Technol.* **1986**, *A9*, 2386.
- (16) Berland, B. S.; Brown, D. E.; Tolbert, M. A.; George, S. M. *Geophys. Res. Lett.* **1995**, *22*, 3493.
- (17) Haynes, D. R.; Tro, N. J.; George, S. M. *J. Phys. Chem.* **1992**, *96*, 8502.
- (18) Benson, S. V.; Schultz, J.; Hooper, B. A.; Crane, R.; Madey, J. M. *J. Nucl. Instrum. Methods* **1988**, *A272*, 22.
- (19) Benson, S. V.; Fann, W. S.; Hooper, B. A.; Madey, J. M. J.; Szarmes, E. B.; Richman, B.; Vintro, L. *Nucl. Instrum. Methods* **1990**, *A296*, 110.
- (20) Wood, B. E.; Roux, J. A. *J. Opt. Soc. Am.* **1982**, *72*, 720.
- (21) Toon, O. B.; Tolbert, M. A.; Koehler, B. G.; Middlebrook, A.; Jordan, J. *J. Geophys. Res.* **1994**, *99*, 25631.
- (22) Vodopyanov, K. L. *J. Chem. Phys.* **1991**, *94*, 5389.
- (23) Vodopyanov, K. L. *Sov. Phys. JETP* **1990**, *70*, 114.
- (24) Iogansen, A. V.; Rozenberg, M. Sh. *Opt. Spectrosc.* **1978**, *44*, 49.
- (25) Brand, J. L.; George, S. M. *Surf. Sci.* **1986**, *167*, 341.
- (26) Carnahan, B.; Luther, H. A.; Wilkes, J. O. *Applied Numerical Methods*; John Wiley and Sons: New York, 1969.
- (27) Fletcher, N. H. *The Chemical Physics of Ice*; Cambridge University Press: London, 1970.
- (28) Redhead, P. A. *Vacuum* **1962**, *12*, 203.